

***P* and *S* wave velocity and V_P/V_S in the wake of the Yellowstone hot spot**

Derek L. Schutt¹

Department of Terrestrial Magnetism, Carnegie Institution of Washington, Washington, DC, USA

Eugene D. Humphreys

Department of Geological Sciences, University of Oregon, Eugene, Oregon, USA

Received 10 February 2003; revised 24 August 2003; accepted 24 September 2003; published 17 January 2004.

[1] Seismic V_P , V_S , and V_P/V_S structure is imaged across the Yellowstone hot spot swell, including the hot spot track where magmatism occurred at the eastern Snake River Plain ~ 6 – 10 m.y. B.P. Data are teleseismic P and S travel time delays that have been corrected for the well-understood upper mantle anisotropy and crustal structure. Amplitude variations in the imaged structures are 6.2%, 11.2%, and 8% for V_P , V_S , and V_P/V_S , respectively. The dominant structure is a zone which extends beneath the Snake River Plain to a depth of ~ 190 km that is high in V_P/V_S and low in V_P and V_S . The physical state of the upper mantle is inferred by assuming isostasy, using the volume of melt segregated from the mantle that is inferred from estimates of magma addition to the crust, and using relations that scale changes in temperature, partial melt fraction and composition to density. Specifically, we infer that the low-velocity mantle beneath the Snake River Plain is partially molten up to 1.0%, and the high-velocity Yellowstone swell mantle away from the Snake River Plain is $\sim 80^\circ$ K cooler and $\sim 5\%$ depleted in basaltic component. The imaged large seismic velocity variations occur under near isothermal conditions. *INDEX*

TERMS: 7218 Seismology: Lithosphere and upper mantle; 8120 Tectonophysics: Dynamics of lithosphere and mantle—general; 8124 Tectonophysics: Earth's interior—composition and state (1212); 8180 Tectonophysics: Tomography; 9350 Information Related to Geographic Region: North America; *KEYWORDS*: Yellowstone, tomography, V_P/V_S , hot spot, Snake River Plain, upper mantle

Citation: Schutt, D. L., and E. D. Humphreys (2004), P and S wave velocity and V_P/V_S in the wake of the Yellowstone hot spot, *J. Geophys. Res.*, 109, B01305, doi:10.1029/2003JB002442.

1. Introduction

[2] Yellowstone is the most prominent and best known continental hot spot. As it propagated across eastern Idaho to its current location in NW Wyoming, it left behind a swath of magmatically altered crust, the eastern Snake River Plain (SRP), which lies along the axis of a SW broadening wake-like swell. This behavior is consistent with mantle melt release at a focused site that is stationary in a hot spot reference frame, and with the hot and buoyant residuum flattening against the base of the lithosphere as it is dragged to the SW by North America plate motion.

[3] A line array of seismometers crossing the swell and SRP where the hot spot was about 6–10 m.y. B.P. provided the teleseismic data that are the basis for several studies, including ours (Figure 1). Seismically inferred crustal structure beneath this array allows the crustal load on the mantle to be estimated [Peng and Humphreys, 1998];

assuming isostasy, the mantle is calculated to be uniformly very buoyant across the width of the swell, and approximately of normal continental buoyancy southeast of the swell. Split *SKS* arrivals recorded by this array indicate that across the width of the swell there exists a simple mantle anisotropy aligned nearly in the direction of North America plate transport [Schutt *et al.*, 1998]. This stands in contrast to the pattern of anisotropy away from the swell, which is more complex [Schutt and Humphreys, 2001]. These findings are consistent with a mantle plume origin for Yellowstone.

[4] Upper mantle P wave velocity is found to be anomalously slow only beneath the SRP [Evans, 1982; Dueker and Humphreys, 1990], whereas mantle beneath the remainder of the swell is fast compared to average western U.S. upper mantle and rather typical of global average upper mantle [Humphreys and Dueker, 1994]. The zone of low-velocity upper mantle extends to depths of at least 200 km [Saltzer and Humphreys, 1997]. Using seismic velocity and buoyancy estimates, they interpret the low-velocity mantle to be partially molten.

[5] While melt at such great depths has been considered unreasonable [e.g., McKenzie and Bickle, 1988], imaging beneath other areas also has revealed low-velocity zones

¹Now at the Department of Geology and Geophysics, University of Wyoming, Laramie, Wyoming, USA.

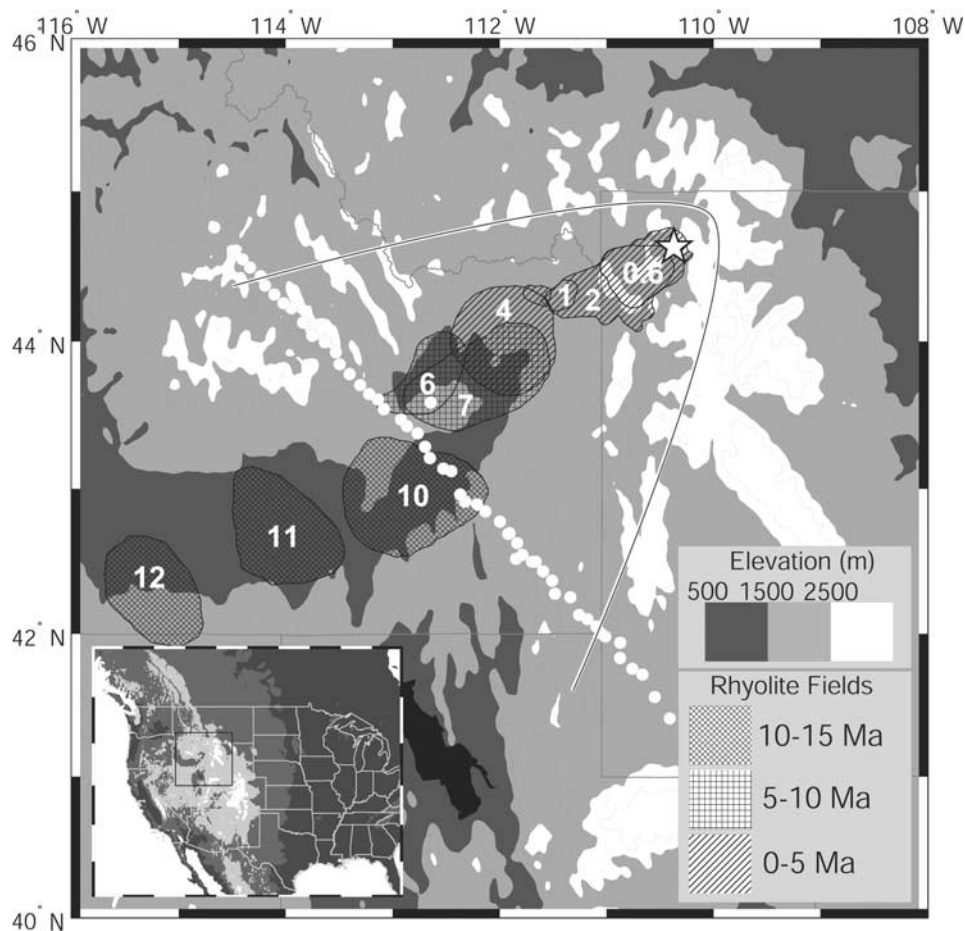


Figure 1. Station locations and tectonic setting of our study. A northeast younging series of rhyolite fields in southern Idaho (patterned areas, ages in Ma), shows the Yellowstone Hot spot track. White circles show the locations of 54 seismometer sites. Parabolic line indicates the margin of the Yellowstone swell (the outer “tectonic parabola” of *Anders et al.* [1989]). Basaltic crustal intrusion along the hot spot track loads the crust, creating the topographically depressed eastern Snake River Plain. The seismic array spans the entire swell.

interpreted to be partially molten mantle [e.g., *Toomey et al.*, 1998]. In our study we use the combined P and S wave data to address the issue of partial melt directly with seismic methods, avoiding a reliance on indirect arguments. Our data set is ideal for this purpose because high-quality P and S wave data are available along a long transect that trends across a strong and isolated low-velocity volume.

2. P and S Wave Velocity Structure

2.1. Data

[6] In 1993, 54 sites occupied by 25 three-component seismometers provided the data for our investigation. Except for three high-frequency L4c seismometers, the seismometers were CMG3-ESP or STS2 broadband instruments made available by the Program for Array Seismic Studies of the Continental Lithosphere (PASSCAL). The seismic sites formed a 550-km-long NW oriented line array across the entire Yellowstone swell, and extended approximately 100 km SE of the swell into SW Wyoming (Figure 1).

Initial P wave processing was done by Rebecca Saltzer, as described by *Saltzer and Humphreys* [1997]. We use these P wave travel time picks in our analysis. S wave data were processed as part of this project, as described below.

[7] The 54 stations recorded 932 usable S waves from 59 teleseismic events over the 6 month duration of field deployment P and S ray distribution is shown in Figure 2. Data were sampled at 10 or 20 Hz, and processed using standard techniques including adjusting for clock errors, deconvolving instrument response, and phaseless band-pass filtering between 0.02 and 1 Hz with a six-pole Butterworth filter. P and S waveforms for each event were time shifted using the IASP91 Earth model [*Kennett*, 1995], and these delays were then corrected for elevation, sediment thickness and crustal structure. Crustal corrections were calculated using the crustal structure estimated at each seismic station by *Peng and Humphreys* [1998], whose receiver function analysis incorporated results from the reflection-refraction investigation of *Sparlin et al.* [1982].

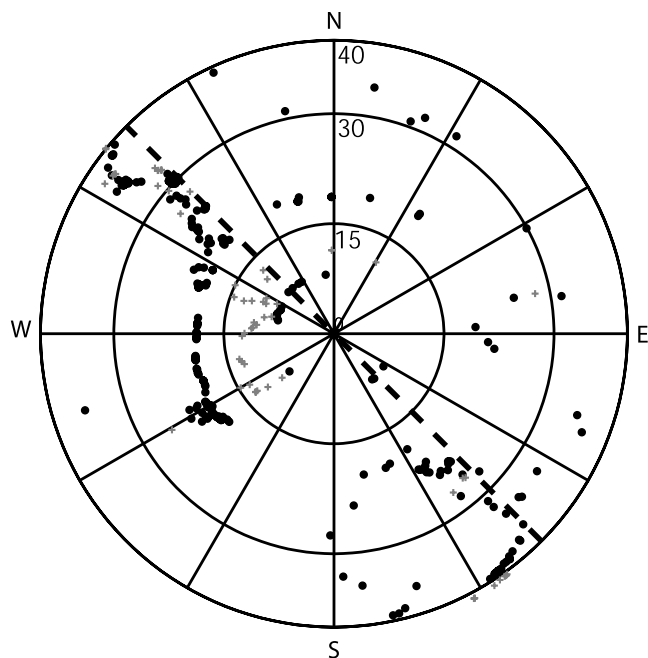


Figure 2. Ray angle of incidence and back azimuth for P waves (solid circles) and S waves (gray pluses). One symbol is plotted for each P or S event. Angle of incidence is calculated from ray parameter, assuming a P wave velocity of 8 km/s and S wave velocity of 4.6 km/s.

[8] To minimize complicating effects of anisotropy on the S waveforms, they were rotated into a $N60^\circ E$ reference frame. This is the average fast axis orientation across the entire array, and all fast axes across the Yellowstone swell are close to this orientation [Schutt *et al.*, 1998]. Because the anisotropy structure is very simple (i.e., it is modeled well by a layer of simply sheared mantle) and nearly uniformly aligned across the entire array [Schutt *et al.*, 1998], rotation to obtain the fast axis arrivals produces waveforms that are nearly free of the slow arriving wave. For each event, the rotated fast axis waveforms are very similar to one another across the array. This correction allowed us to use cross correlation on the first S wave peak of the fast axis traces to accurately estimate travel time residuals for the fast axis arrivals. This was accomplished with an iterative scheme in which, for each event, traces were aligned on the first peak and summed, and then recorrelated with the summed trace to obtain an updated estimate for the residuals. The realigned traces were summed again to obtain an improved reference trace, which was used for an improved cross correlation. This process was repeated until time adjustments for all traces were less than 0.1 s.

2.2. Travel Time Corrections for Crustal Structure and Anisotropy

[9] We apply two sets of travel time corrections to our data. First is a station statics correction, which accounts for crustal structure not resolved by receiver function work of Peng and Humphreys [1998]. After an initial inversion for velocity structure, we calculate P wave statics by finding the mean difference between actual and model-predicted travel

times for rays arriving at each station. The average absolute value of station statics is 0.096 s (station statics have a mean of 0). We then subtract these statics from our travel time data and reinvert for P wave structure. The reason we calculate station statics following the initial inversion is to account for delay with earth structure (and minimize station statics) as much as possible. Because P wave statics are better resolved than S wave statics, we multiply the P wave statics by $\sqrt{3}$ to obtain estimates of S wave statics.

[10] The second travel time adjustment corrects for effects of anisotropy. Our goal in tomographic imaging is to estimate isotropic P and S velocities (i.e., velocities averaged over all solid angles), which requires correcting our teleseismic delays for known effects of anisotropy. SKS splits and null arrivals observed at our stations have a simple behavior that indicate a uniform $\sim N60^\circ E$ orientation of fast axes [Schutt *et al.*, 1998]. This is consistent with olivine alignment caused by expected simple shear strain in the hot spot mantle [Schutt *et al.*, 1998]. The effect of anisotropy with a horizontal fast axis is to delay teleseismic arrivals. SKS split times δt vary from 0.6 to 1.6 s, implying variable delaying effects owing to variable amounts of anisotropy.

[11] Using the simplest representation of anisotropy that is consistent with SKS splitting observations, we assume that anisotropy is described by an olivine elasticity tensor with a horizontal a axis oriented $N60^\circ E$. We assume half the b axes are aligned vertically (horizontal symmetry) and the remaining half are randomly aligned (orthogonal symmetry). The orientation of the b and c axes, however, make little difference, as described below.

[12] We determine travel time corrections for anisotropic structure through a two step process. We first map variations in split time to perturbations in anisotropy structure under each station, then use these perturbations to estimate travel time corrections.

[13] Assuming uniformly aligned anisotropy beneath each station [Schutt *et al.*, 1998], variations in split time are caused by some combination of changes in intensity of anisotropy and changes in thickness of the anisotropic layer. SKS splitting data alone cannot distinguish between the two; however, their travel time effects are nearly identical.

[14] We choose to calculate anisotropic effects with perturbations in anisotropic intensity $\phi = (V_{S_{fast}} - V_{S_{slow}}) / V_{S_{iso}}$, where $V_{S_{fast}}$ and $V_{S_{slow}}$ refer to the velocities of vertically propagating fast and slow quasi-shear waves, and $V_{S_{iso}}$ is the S wave velocity that would exist if the mantle were isotropic. Our reference anisotropic layer is 135 km thick and has $\phi = 4\%$, which produces the observed mean split time of 1.29 s [Schutt *et al.*, 1998]. We then seek perturbations in anisotropy intensity $\Delta\phi$ that produce the observed variations in split time.

[15] ϕ is calculated by Voight averaging proportions of an isotropic and an anisotropic elasticity tensor so as to produce the observed split time. We use the $1300^\circ K$ tensor values for olivine from Isaak *et al.* [1989] in our calculations. Our isotropic tensor is obtained by Voight averaging this tensor over all solid angles. The maximum anisotropic tensor is obtained by Voight averaging equal proportions of the hexagonal and orthorhombic assumptions of olivine alignment (i.e., between randomly and uniformly aligned

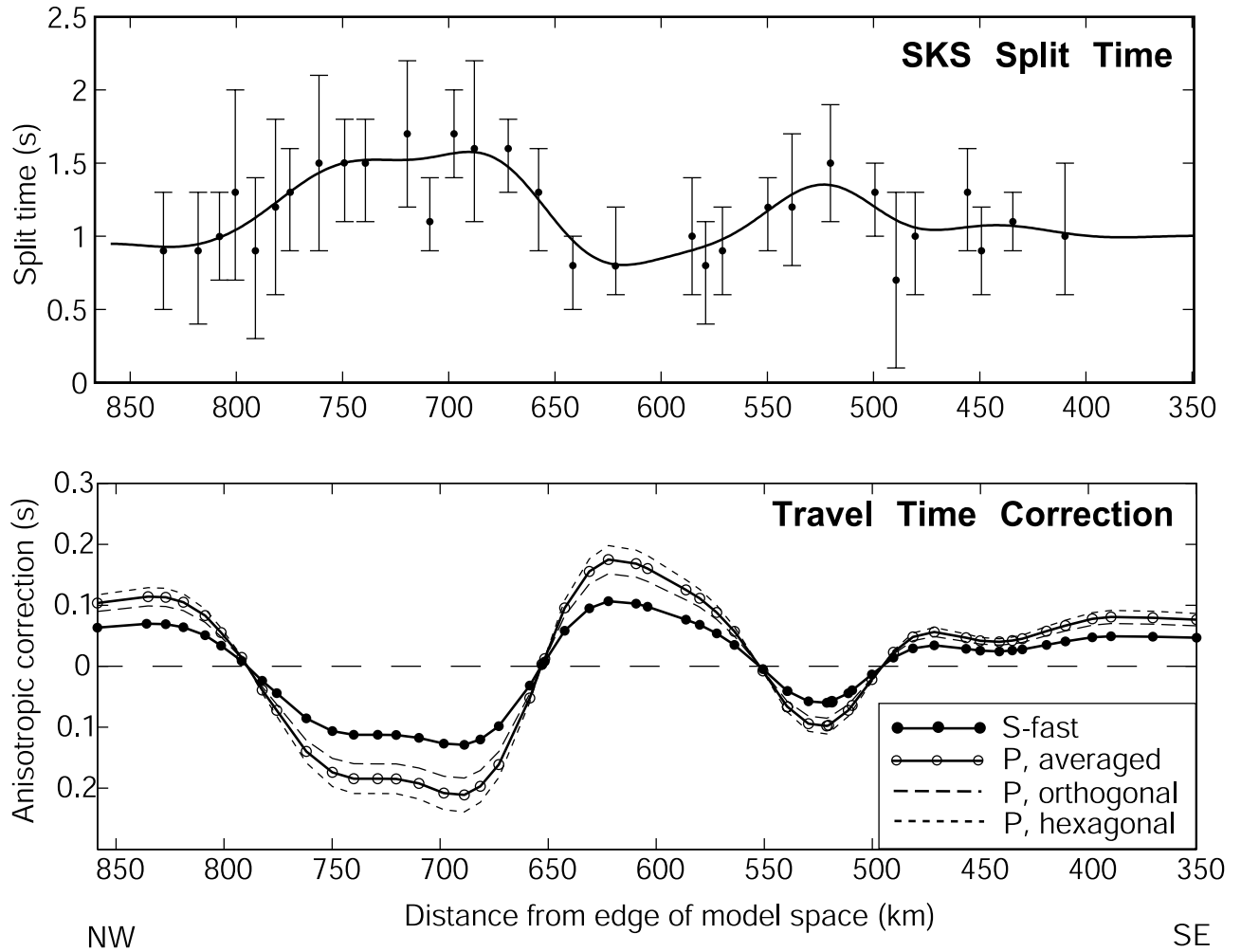


Figure 3. Station travel time corrections for anisotropy. (top) Station averaged S wave split times, with 2σ error bars. Line shows spatially low-passed average of splitting times used for anisotropy corrections. (bottom) Travel time corrections applied to each station for S waves (solid circles) and P waves (open circles). Both orthogonal and hexagonal assumptions for olivine alignment were considered. For S waves the difference in travel time correction is insignificant. For P waves the results of each assumption are shown. Final P wave corrections are the average of these assumptions. Horizontal axis shows station distance from edge of model space, as projected on a NW-SE trending line.

b axes), though in our application, it makes little difference whether we use a hexagonal or orthorhombic tensor.

[16] With these assumptions,

$$\Delta\phi = 0.029(\Delta\delta t) \quad (1)$$

where $\Delta\delta t$ is the deviation in split time from 1.29 s. Vertical wave speed then varies with ϕ as

$$V_P = V_{P_{\text{iso}}} - 7.24(\Delta\phi) \quad (2a)$$

$$V_{S_{\text{fast}}} = V_{S_{\text{iso}}} - 1.50(\Delta\phi) \quad (2b)$$

$$V_{S_{\text{slow}}} = V_{S_{\text{iso}}} - 5.97(\Delta\phi). \quad (2c)$$

[17] The coefficients in this relation do not change appreciably for rays with back azimuths along the strike

of the array propagating up to 30° off vertical. The few significantly off vertical rays that come in perpendicular to the array strike would see higher velocities, but there are too few of these rays to affect the resulting velocity image. Equations (1) and (2) combine to yield

$$\Delta t_P = 0.50(\Delta\delta t) \quad (3a)$$

$$\Delta t_S = 0.31(\Delta\delta t). \quad (3b)$$

[18] Application of these travel time adjustments compensate well for the effects of anisotropy, thereby providing estimates of teleseismic delays through an upper mantle of equivalent isotropic velocity (Figure 3).

2.3. Inversion

[19] The travel time residuals (Figure 4) are inverted for velocity structure using the Simultaneous Iterative Reconstruction Technique (SIRT) algorithm [Humphreys and

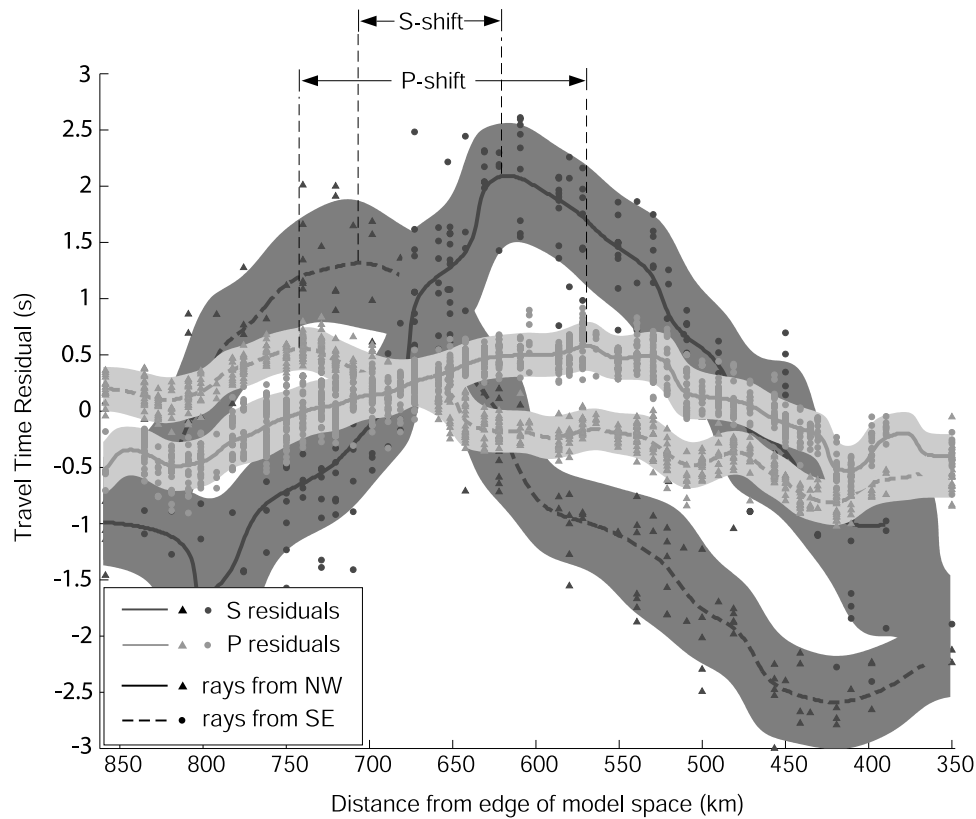


Figure 4. P and S wave travel time residuals, plotted against distance. Residuals of P and S rays coming from the NW are plotted as gray and solid triangles; mean residual trend (spatially averaged) for these rays is indicated by the gray and solid lines. Residuals for rays from the SE are plotted as gray and solid circles, and residual trends are indicated by dashed line. Solid regions around residual trends graphically indicate distribution of residuals. Only residuals from rays in a NW-SE trending vertical plane through the array (having piercing points at 400 km depth that are no more than 100 km horizontally from a line through the array), and with angles of inclination greater than 15° are plotted. Note that the shift in residual trend is larger for the P residuals than for the S . This suggests the P velocity anomaly is located deeper than the S anomaly. Distance on horizontal axis is defined as in Figure 3.

Clayton, 1988; Nolet, 1993]. Ray paths were calculated using Snell's law to guide rays through *Grand's* [1994] tectonic North America radial velocity structure. *Saltzer and Humphreys* [1997] show that with SRP data, choice of reference radial velocity structure and use of 3-D ray tracing make only imperceptible differences in inversion results. They also show that for the upper mantle structure beneath this array, differences between inversions produced by the SIRT and LSQR algorithms are inconsequential [*Paige and Saunders*, 1982].

[20] The seismic array is a line oriented toward the back azimuths of most global seismicity, and it trends perpendicular to the hot spot track and known upper mantle structure (Figure 5) [*Evans*, 1982; *Humphreys and Dueker*, 1994]. This deployment geometry is designed to provide a high-resolution 2-D cross section across the Yellowstone swell perpendicular to the SRP. The tomographic model (Figure 5) is aligned with the seismic array. It extends 1200 km in the direction of the array (i.e., $N45^\circ W$), is 200 km wide in the cross-array direction, is centered on the SRP, and extends to a depth of 450 km. The model consists of blocks 10 km deep and 10 km wide in the direction of the array. Blocks extend 200 km to the SW of the array. This model geometry

provides a 2-D inversion for structure SW of the array, through which most of the rays travel. Structure to the NE of the array is similar, but resolution is poorer, and we confine our study to the SW volume. Ray coverage is shown in Figure 6. Figure 7 shows results of straightforward inversion of the anisotropy-corrected S wave travel time residuals, using the Simultaneous Iterative Reconstructive Technique (SIRT) [*Gilbert*, 1972; *Humphreys and Clayton*, 1988]. Results are similar if data are limited to nearly vertical rays and rays with back azimuths along the strike of the array.

[21] A prominent low-velocity zone is imaged beneath the center of the array extending from the surface to about 200 km in depth. The NW dip of the low-velocity zone is thought to be authentic because inversions of synthetic rectangular-shaped vertical structures do not produce dipping structures. With our teleseismic rays, which all arrive within 40° of vertical, the horizontal position of the low-velocity body is well resolved (Figures 8a and 8b). Application of anisotropy corrections have a small but noticeable effect on imaged structure. They do not change overall character of inversion or any of the findings discussed below.

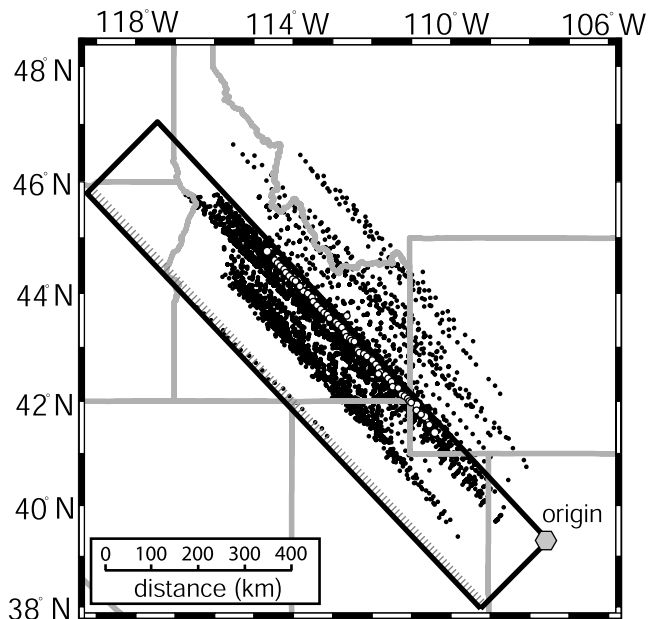


Figure 5. Modeled volume of tomographic inversion. Modeled volume is 800 km long, 200 km wide (outline shown with heavy lines), and 450 km deep. Model blocks are indicated with the thin tick marks. In this study we consider structure to the SW side of the array. Individual model blocks are 10 km wide (NW-SE), 15 km deep, and extend 200 km in the NE-SW direction. Solid circles are ray piercing points at 300 km depth. Open circles are station locations. Origin used for distance measurements marked with a hexagon.

[22] In contrast to excellent horizontal resolution, vertical resolution of structure is relatively poor. This is a result of vertical “streaking,” which is well understood to be the primary resolution problem in upper mantle teleseismic tomography. Streaks are artifacts extending away from actual structures in directions commonly taken by rays (Figures 7, 8a, and 8c), often with increases in amplitude where the streaks meet the boundaries of the model. More precisely, streaks occur where a lack of crossing rays results in a model that is locally underdetermined, and a broadly distributed feature is produced by the implicit tendency of inversion to create a model of minimum energy (in addition to any other constraints being imposed). *Keller et al.* [2000] and *Wolfe et al.* [2002] discuss this resolution problem with respect to imaging beneath Iceland. The low-velocity streaks that trend away from the prominent low-velocity structure beneath the SRP (at $\sim 30^\circ$ from vertical) are typical of these artifacts. This is confirmed by testing resolution of structures confined in the uppermost mantle beneath the SRP, which produce similar streaks upon inversion.

[23] To assess our ability to resolve the depth limits of the SRP low-velocity zone, we make use of vertical “squeezing” experiments that test the need for structure outside of specified depth limits [*Saltzer and Humphreys, 1997*]. The principle is to hypothesis test for permissibility of a depth limit constraint by testing if any information in the data is significantly in contradiction with the constraint. In our

tests, we invert data in a normal fashion except that structure is allowed only within a specified depth range (e.g., only between 90 and 150 km). This constraint is then relaxed and structure is allowed to be reconstructed throughout the model. The initial depth-constrained inversion results in the least squares best model within the prescribed depth range, which we term the “initial model domain”, and it yields travel time residuals with respect to this model. These residuals (which cannot be explained by the depth-constrained model) are themselves inverted for structure in the full model space and added to the original model, just as is normal for an additional SIRT inversion. If all residuals were zero, we produce no new structure; if the residuals are random values, then we would produce essentially no new structure. Only if a better model exists (in a least squares sense) is the updated structure different from the initial structure, and this is recognized by the inclusion of significant structure outside the initial model domain. An example of a squeezing test on synthetic data is shown in Figures 8a and 8b.

[24] To test the need for near surface and deep structure, we run two series of squeezing tests. In each series of tests, we invert for structure within the initial model domain using 5 SIRT iterations, then extend the area of allowed structure into the whole model space for 15 more iterations. In these tests, the initial model domain is above 300 km, which is the greatest depth for which there are crossing rays, and hence relatively good resolution.

[25] The first series of inversions test the necessity of near surface structure. We test a range of depths for the top of the initial model domain ranging from 30 to 210 km in 10 km intervals, with the bottom held at 300 km, and look for coherent near-surface structure to develop after we relax the squeezing constraint. When the top of the initial model domain is located below about 80 km, both the P and S inversions develop a coherent low-velocity region above this bound. Thus a model that extends between 80 and 300 km explains the data about as well as possible, but a model with a top deeper than 80 km in depth begins to violate information contained in the data.

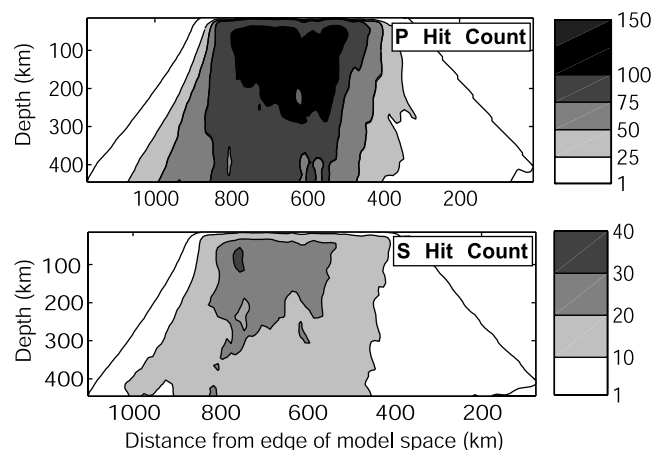


Figure 6. Hit count in model blocks, as represented by total ray length through each block (in km). Region of good crossing ray coverage extends to about 300 km beneath the array center.

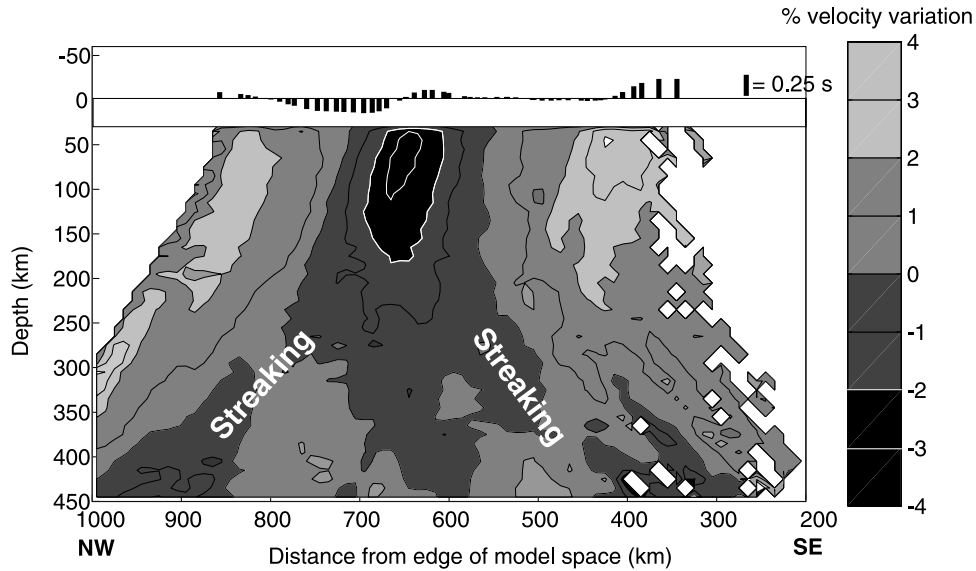


Figure 7. Initial SIRT inversion of S wave data. Contour interval is 1%. Anisotropic corrections are shown at the top. These corrections are small and uncorrelated with the imaged isotropic structure. Since the S wave rays are nearly vertically incident, vertical resolution is limited, causing streaking of velocity features along the paths most commonly taken by rays. The structure labeled streaking are typical of this behavior, and in all likelihood are artifacts.

[26] The second set of squeezing inversions tests for deep structure. We test depths for the bottom of the initial model domain ranging from 100 to 300 km at 10 km intervals, while keeping the top of the domain at 30 km. A low-velocity region appears beneath the bottom of the initial model domain when it is located at a depth above 190 km, indicating that velocity structure extends to at least 190 km (Figure 8c), and is not required beneath this depth.

[27] These squeezing tests indicate that velocity structure necessarily exists between depths of 80 and 190 km. The fact that no structure is required outside of these bounds, combined with the observation that tests on simple synthetic structures outside these bounds can be at least partially resolved, suggests that actual earth structure is largely confined to within these limits.

[28] Figure 9 shows our best estimate of perturbational P and S velocity structure beneath the array, based on an initial model domain extending from 80 to 190 km. P velocity varies by 6.2% in this image, and S velocity varies by 11.2%. Note that our squeezing removes most of the dipping trend of the P low-velocity zone in Figure 7. This image V_P structure is very similar to that obtained by *Saltzer and Humphreys* [1997], indicating that the effects of the anisotropy corrections are relatively minor. The V_S structure differs slightly from the V_P in that the area of low velocity is shallower. We further examine differences between V_P and V_S below.

3. V_P/V_S Structure

[29] Because P and S wave velocities have different sensitivities to partial melt, temperature, and composition, a combination of V_P and V_S provides more insight into mantle physical state than either V_P or V_S alone. In particular, V_S is more sensitive to the presence of melt than is V_P

(while being similarly sensitive to composition and temperature), hence, V_P/V_S can be used to distinguish regions of partial melt. In this section, we first compare the P and S travel time residuals to demonstrate that systematic differences exist between these data sets. We then invert these data for perturbational V_P/V_S structure. Unlike the V_P and V_S tomography inversions, where spatial resolution is maximized, the V_P/V_S inversion is optimized for correct amplitudes. The resulting tomogram will then be used to estimate the physical state of the mantle.

3.1. Comparison of P and S Data

[30] Figure 4 shows P and S travel time residuals for events of opposing back azimuth. The shift in the S wave residual pattern is less than that for P waves, implying that the centroid of the S wave low-velocity zone is shallower than that of the P wave low-velocity zone. Also, the lateral transitions in S delays are greater, implying a greater horizontal velocity gradient near the boundaries of the V_S low-velocity anomaly. To further consider these differences, we compare P and S wave travel time residuals for rays that share common paths. The ratio of the S wave residuals δt_S to the P wave residuals δt_P is related to the material seismic velocities V_P and V_S by [*Hales and Herrin*, 1972]

$$\frac{\delta t_S}{\delta t_P} \approx \frac{\partial \ln V_S}{\partial \ln V_P} \left(\frac{V_P}{V_S} \right). \quad (4)$$

By applying the least squares method [*York*, 1966] to fit lines to the data (using a S residual picking error of 0.4 s, a P picking error of 0.1 s, and assuming V_P/V_S to be 1.82, the IASP91 [*Kennett*, 1995] value at 180 km depth), we find $\partial \ln V_S / \partial \ln V_P$ to be 8% greater for the late arriving rays than the early arriving rays (Table 1). This corresponds to Poisson's ratio increasing from 0.25 to 0.28. Thus the

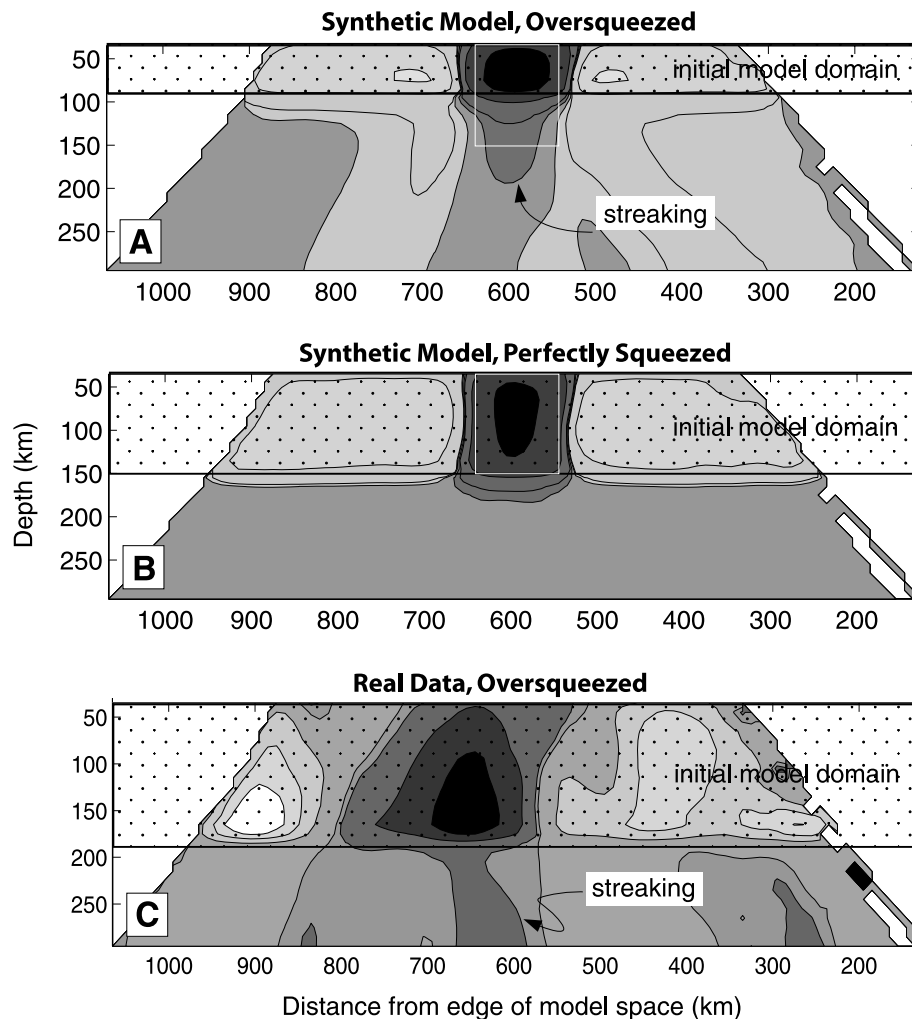


Figure 8. Example of squeezing tests on real and synthetic data. Synthetic delays are calculated using the actual ray set traced through a prescribed structure ($\Delta V = -10\%$ within the white rectangle) and with noise added ($1\sigma = 0.4\text{s}$), and then inverting these delays. Initial inversion is constrained to an initial model domain as shown with the patterned area. Subsequent inversion reconstructs deeper structure if information exists in the residuals for structure that cannot be explained within the initial model domain. (a) Oversqueezed inversion. Downward streaking of imaged velocity anomaly indicates the presence of structure below the initial model domain. (b) Ideally squeezed inversion. Almost no velocity structure appears beneath the initial model domain. (c) Inversion of real data. The initial model domain is set at 180 km, and downward streaking similar to case in Figure 8a is noted, indicating the need for deeper slow mantle beneath the imaged low-velocity mantle. An initial model domain extending to 190 km removes this streaking.

S velocities are depressed compared to the P velocities in the slow mantle beneath our array, as they would be if the low-velocity mantle were partially molten.

3.2. Calculation of Perturbational V_P/V_S Structure

[31] A meaningful comparison of V_P and V_S structures cannot be done without first accounting for differences in the P and S ray coverage. Differing ray coverage will cause differing resolution in the V_P and V_S images, and if V_P is divided by V_S to get V_P/V_S , spurious perturbations will be created. In Figure 10, we show an example of this instability. We trace rays through a synthetic V_P/V_S anomaly, calculate P and S travel time residuals, add noise (0.1 s for P , 0.4 s for S), and invert for V_P and V_S . The top subplot

in Figure 10 shows the input V_P/V_S structure and the middle subplot shows the results of dividing V_P by V_S .

[32] Most of the effects of differing resolution can be eliminated by adopting a summary ray technique [Robertson and Woodhouse, 1995]. We create a uniform set of artificial or summary rays, identical for P and S data. For each summary ray we find the 6 nearest actual P or S rays that travel in the NW-SE trending plane of the array, and average the travel time residuals from these 6 rays. (The choice of 6 was found optimal in tests; in-plane data are defined as in Figure 4). This produces a set of travel time residuals for the summary ray set, which can be inverted to produce perturbational V_P and V_S images with similar resolution. V_P/V_S is estimated by adding the S and P velocity perturbations,

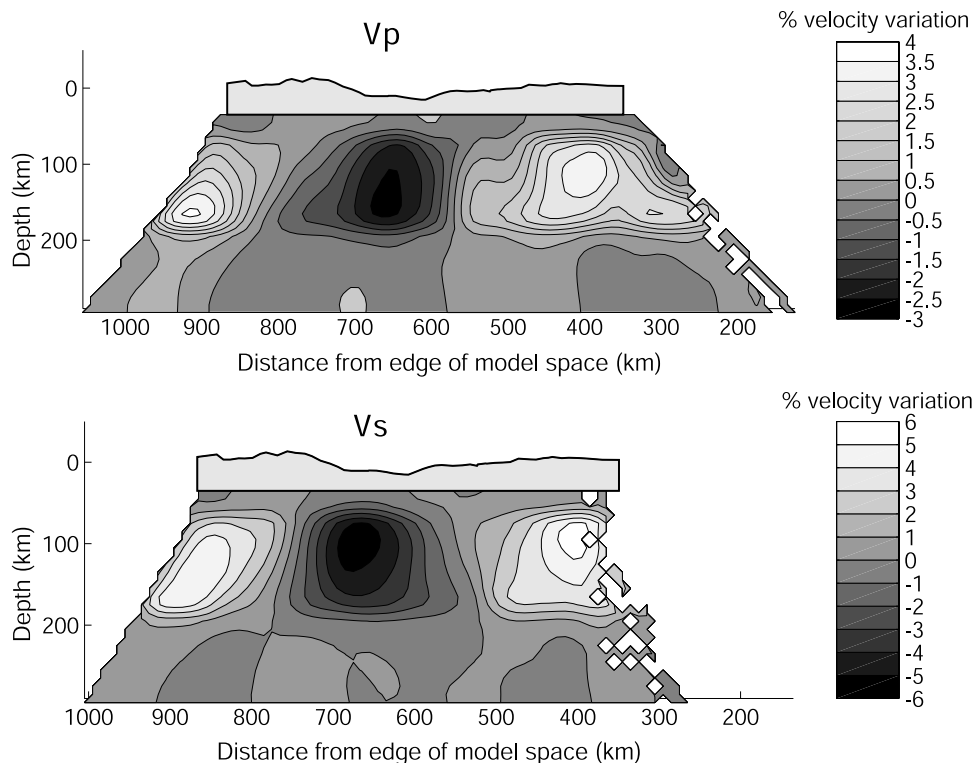


Figure 9. Best SIRT P and S images. Structure is squeezed between 80 and 190 km for 15 SIRT iterations, then squeezing is relaxed for 5 iterations. V_P varies by 6.2%, and explains 59% of the data RMS. V_S varies by 11.2%, and explains 62% of the data RMS. Exaggerated topography (at 25x) is shown above the velocity images. See color version of this figure at back of this issue.

respectively, to the vertical S wave model TNA [Grand, 1994] and $1.82 * \text{TNA}$, and ratioing the resulting velocities. We then remove the mean to produce a perturbational V_P/V_S image.

[33] Summary ray details are shown in Figure 11; this technique essentially smooths the P and S data sets differentially, depending on ray coverage. At 150 km depth, the median horizontal smoothing distance, as defined by the maximum distance between actual rays in the 6 ray set, is 3 km, and the maximum smoothing distance is 57 km. For the S rays the median and maximum smoothing distances are 11 km and 71 km, respectively. In general, smoothing distance is only large near the edges of our model space, and for angles of incidence between 0 and -15° , due to a lack of core phases from the SE.

[34] The summary ray data are inverted using a generalized least squares method. To handle this problem efficiently, we reduced the number of model parameters from that used in the above SIRT inversions. The new model has the same center as the previous inversions, but extends only 800 km in the along the array direction and to 250 km in depth. Also, model blocks are increased in size from $10 \text{ km} \times 10 \text{ km}$ to $15 \text{ km} \times 15 \text{ km}$.

[35] Constraints used in the inversion include horizontal Gaussian smoothing (with a half widths of 30 km), vertical squeezing (a boxcar function lying between 80 and 200 km depth, analogous to the squeezing used in the SIRT inversion), damping to promote stability of the resulting inversion, and the use of high levels of damping of unhit blocks. The intensity of these constraints was adjusted to optimize

inversion of synthetic V_P/V_S test cases, as determined through a grid search. We also investigated the effects of weighting the summary data by a measure of its overall reliability (similar to weighting data by its covariance), and coupling the V_P and V_S inversions [e.g., Michelini, 1993]. However, these constraints were not helpful. Figure 10 shows the effect of the summary ray inversion on a synthetic structure.

[36] Note that in Figure 10, damping has reduced the amplitude of the V_P/V_S anomaly. To account for this effect, we estimate an amplitude correction multiplier. We have produced a synthetic test on a Gaussian-shaped input V_P/V_S anomaly, using the same inversion parameters and find the constant that best fits (in a least squares sense) the inversion V_P/V_S to the synthetic input values. This value is found to be 1.15. We multiply our actual inversion for V_P/V_S structure by this factor to produce our best estimate of the V_P/V_S perturbational amplitude.

[37] Figure 12 shows our best estimate of V_P/V_S structure. V_P/V_S perturbations vary by 8.0%. The predominance of structure near the top of the squeezing band is to be

Table 1. Slope of P Versus S Travel Time Residuals^a

Criteria	Slope	$\partial \ln V_S / \partial \ln V_P$
$t_S > 0$ (late arriving)	3.27 ± 0.08	1.80 ± 0.04
All residuals	3.13 ± 0.08	1.72 ± 0.05
$t_S < 0$ (early arriving)	3.00 ± 0.09	1.65 ± 0.05

^aUncertainties given at 1σ .

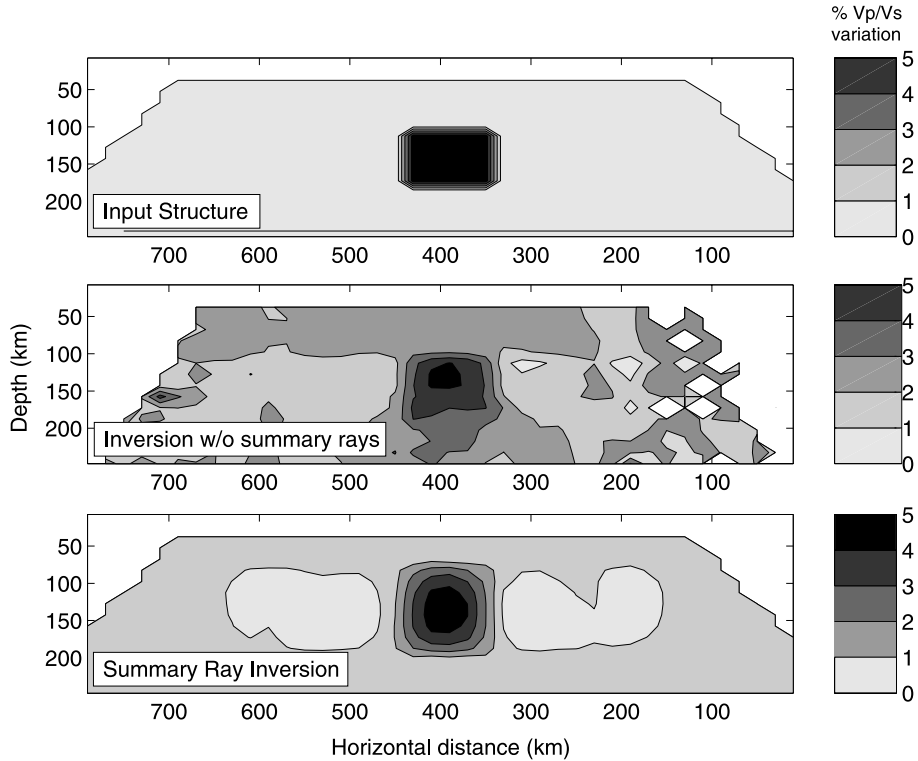


Figure 10. Synthetic V_P/V_S images. Contours at 1%. (top) Input structure. (middle) Inversion without summary rays. This suffers from spurious perturbations due to differences in P and S ray coverage. (bottom) Damped least squares inversion of summary rays. Both inversions have been multiplied by the least squares constant that best fits them to the input structure. They have also been squeezed to between 100 and 180 km. See color version of this figure at back of this issue.

expected since the V_S low is shallower than the V_P low (Figure 4).

3.3. Estimating Mantle Physical State

[38] By applying relationships scaling seismic parameters to mantle physical state, and using constraints based on mantle buoyancy, we estimate the degree of melting, temperature variation and compositional variation of the Yellowstone swell mantle.

[39] Accounting for the large variations in V_P and V_S requires the presence of partial melt beneath the Snake River Plain. However, imprecise knowledge of the V_P and V_S mantle structure prevents the direct seismic identification of the solidus. To estimate degree of melting, we assume that only mantle beneath the Snake River Plain contains melt. This is consistent with the occurrence of crustal features created by large amounts of melting, which all occur near the Snake River Plain [e.g., Peng and Humphreys, 1998]. Using this assumption, the V_P/V_S perturbational contour of 0.5% best spans the width of the Snake River Plain. We use this V_P/V_S value as a proxy for the solidus location. V_P/V_S perturbations above the solidus are nearly entirely caused by variations in melt content [Hammond and Humphreys, 2000]. Using the scaling relations given by Hammond and Humphreys [2000], the V_P/V_S structure shown in Figure 12 implies a maximum of 1.0% melt fraction, with a mean of 0.4%.

[40] V_P/V_S structure in the subsolidus regions are caused by variations in temperature and composition. Mantle

beneath the Yellowstone swell is thought to be buoyant relative to mantle away from the swell [e.g., Anders and Sleep, 1992], as evidenced by the presence of the swell. Yet the upper mantle that is beneath the swell and away from the Snake River Plain is not seismically slow, as would be expected if its buoyancy were attributed simply to elevated temperature. Indeed, on a global scale, it is fast; travel time residuals for this region are faster than the mean residual in the International Seismological Center (ISC) catalog (and travel time residuals for rays traveling under the Snake River Plain are slower than average) [Humphreys and Dueker, 1994]. Saltzer and Humphreys [1997] and Humphreys et al. [2001] use this distinctive fast but buoyant relation to argue that this mantle has been compositionally altered by depletion of a basaltic component.

[41] To estimate the amount of basalt removed, we can compare the region of the tomogram where depletion is indicated with the thickness of basaltic layers in the crust. Weight fraction of melt removed can be estimated with

$$\phi = \frac{V_b \rho_b}{V_d \rho_d}, \quad (5)$$

where V_b and V_d are the volume of basalt and depleted mantle, respectively, and ρ_b/ρ_d is the density ratio between basaltic melt and parent mantle (at the pressure and temperature conditions at which melting took place). We use 0.932 for this density ratio [Schutt et al., 2002].

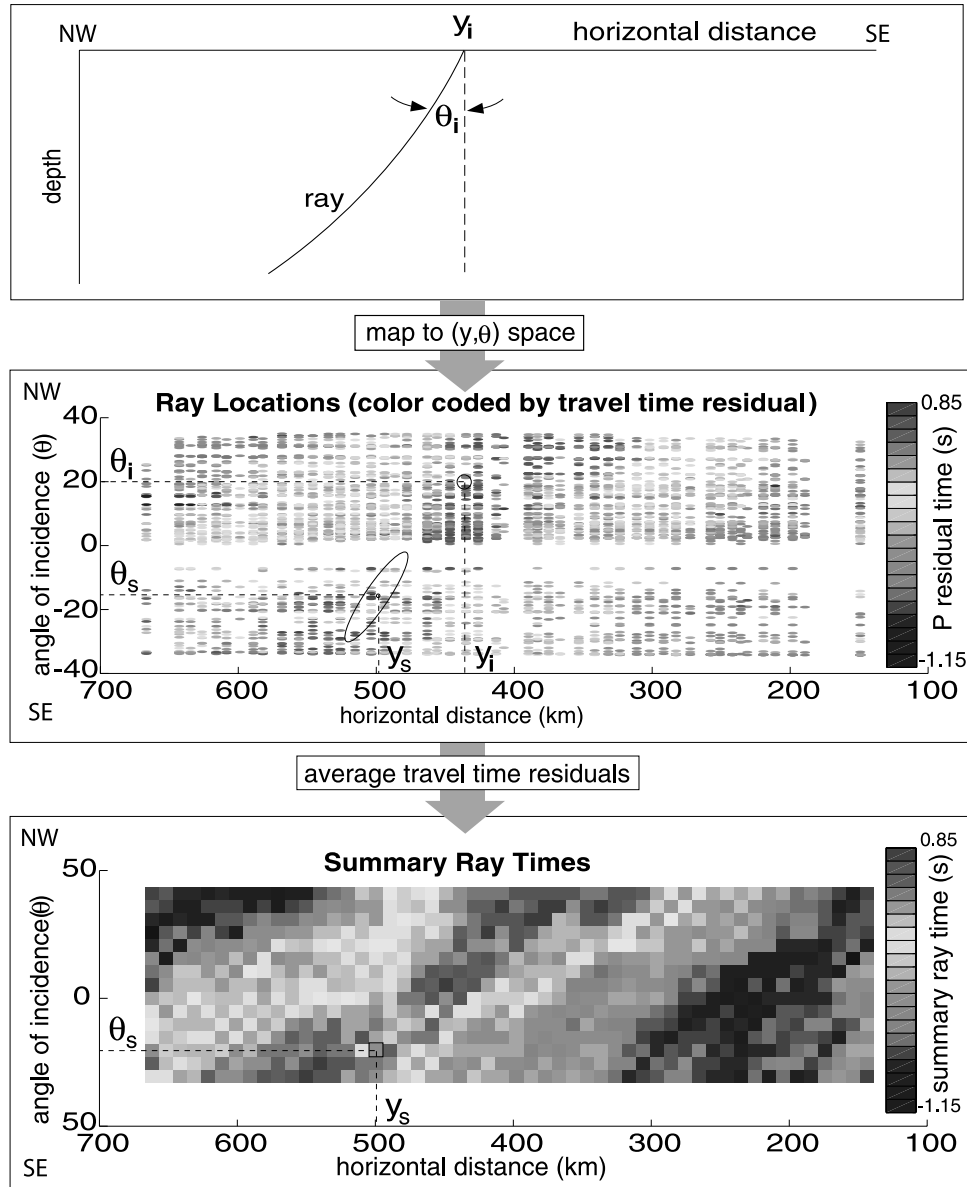


Figure 11. Summary ray travel time calculation. (top) The i th seismic ray, at surface location, y_i , and incidence angle at 30 km, θ_i . (middle) Each ray is mapped to (y, θ) space. Color indicates travel time residual for each ray. Travel times are assigned to summary rays by averaging residuals within an elliptical area around each summary ray (as shown schematically for summary ray at (y_s, θ_s)). (bottom) Delays for each summary ray. See color version of this figure at back of this issue.

[42] We estimate the volume of basalt in a 1 km wide vertical slab extending below the seismic array to be $V_b = 1700 \pm 550 \text{ km}^3$, which includes basalt in surface flows, a large partially basaltic sill, and in crustal underplate (Table 2) [Peng and Humphreys, 1998]. If the low V_P/V_S regions in the mantle correspond to depleted mantle, then $V_d = 33800 \pm 10400 \text{ km}^3$ (Table 3). Equation (5) then yields $\phi = 5.0 \pm 2.5\%$.

[43] To constrain the temperature variation across the array, we use the observation of Peng and Humphreys [1998] that the mantle beneath the swell is uniformly buoyant to within ± 300 m of surface elevation. This implies the buoyancy effects of partial melting, melt depletion, and temperature must nearly balance. We consider two mantle

buoyancy regions: one where partial melt contributes to buoyancy and another where only depletion and temperature contribute to buoyancy (Figure 12). Then,

$$u_M = u_D + u_T \pm 300\text{m}, \quad (6)$$

and

$$u_T = u_M - u_D \pm 300\text{m}, \quad (7)$$

where u_x indicates uplift resulting from x , for x being temperature T , melt M , or depletion D . Uplift can be calculated assuming isostasy,

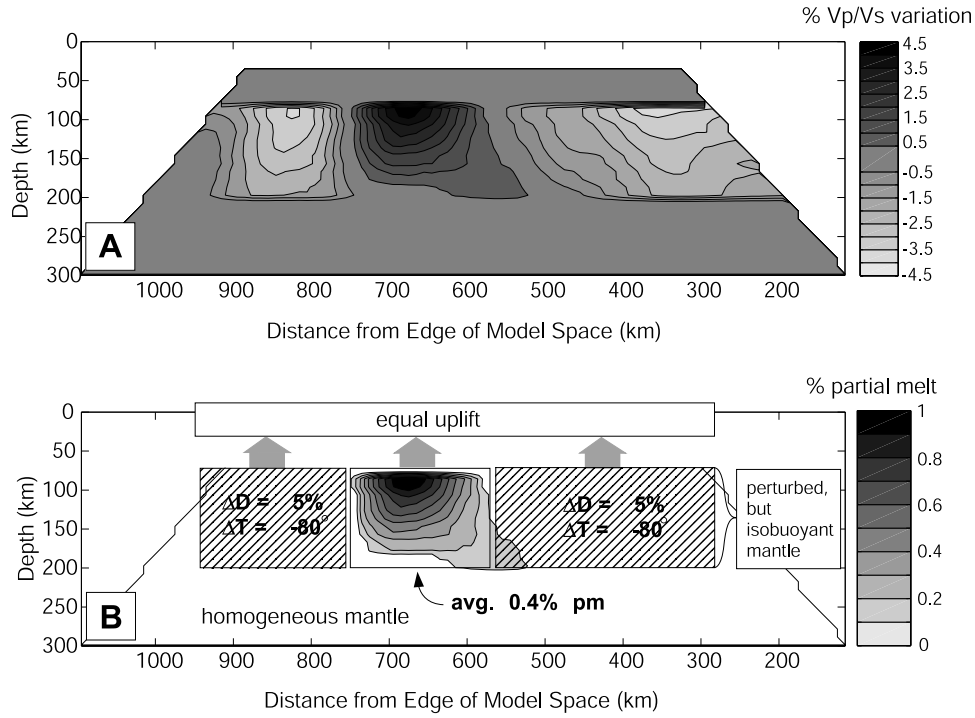


Figure 12. (a) V_P/V_S perturbation. Contours are in 0.5% intervals (the 0% contour is omitted to avoid the visual distraction of noise). Total range of perturbations is 8.0%. Assuming average V_P/V_S is 1.82, actual V_P/V_S varies from 1.75 to 1.90. To produce optimal estimation of amplitude, image has been squeezed and multiplied by a least squares constant based on damping value. (b) Physical state. On the basis of the V_P/V_S structure, we estimate the amount of partial melt to be as much as 1.0% (darkest red region), and to average 0.4% within the central rectangle. The low V_P/V_S areas are melt depleted, and we estimate these regions (approximated by the blue-lined rectangles) to have had 5% melt removal. Since the mantle is isobuoyant, uplift due to depletion and thermal variations must balance uplift due to partial melting. This suggests that the regions indicated by the blue-lined rectangles are, on average, 80° colder than the region containing partial melt. See color version of this figure at back of this issue.

$$u_x \approx -l \left(\frac{\partial \ln \langle \rho \rangle}{\partial x} \right) \Delta x \quad (8)$$

for l being the thickness of the layer being considered and $\langle \rho \rangle$ being the mean density of this layer. Combining (7) and (8) gives

$$\Delta T = \left(\frac{\partial \ln \langle \rho \rangle}{\partial T} \right)^{-1} \left[\frac{\partial \ln \langle \rho \rangle}{\partial M} \Delta M - \frac{\partial \ln \langle \rho \rangle}{\partial D} \Delta D \pm \frac{300 \text{m}}{l} \right] \quad (9)$$

for ΔT being the temperature difference between the partially molten region and the depleted region, $\Delta D = \phi = 0.005$ is the amount of depletion, $\Delta M = 0.004$ is the mean melt fraction, and $l = 110$ km is the thickness of anomalous mantle. The sensitivity derivatives

$$\frac{\partial \ln \langle \rho \rangle}{\partial T} = -3.685 \times 10^{-5} \text{ } ^\circ\text{K}^{-1} \quad (10a)$$

$$\frac{\partial \ln \langle \rho \rangle}{\partial D} = -7.025 \times 10^{-2} \quad (10b)$$

$$\frac{\partial \ln \langle \rho \rangle}{\partial M} = -1.391 \times 10^{-1} \quad (10c)$$

are calculated from the work of Schutt *et al.* [2002], assuming temperature change, depletion level change, degree of partial melting, and mantle composition are constant from 80 to 190 km depth (the depth range in which we suppose structure to exist). Putting these together, we find $\Delta T = 80^\circ \pm 90^\circ$, to be the difference in average temperature between the central low-velocity region and the high-velocity sides. Although the error is large, it is likely the Yellowstone Swell mantle is nearly isothermal. This value is consistent with the velocity-temperature scaling of Karato [1993], if Q_S at the solidus is 20 or lower.

4. Conclusions and Discussion

4.1. Seismic Investigation

[44] Our seismic investigation of P and S wave travel time data recorded across the Yellowstone swell provides

Table 2. Estimation of Basalt Volume

Location	Width, km	Thickness, km	Area, km ²
Surface	70 ± 10	2 ± 1	140 ± 120
Sill ^a	90 ± 10	10 ± 2	900 ± 220
Underplate	170 ± 30	4 ± 1	680 ± 210

^aSill is approximately half basalt; the area reflects this. Measurements are estimated from Peng and Humphreys [1998].

Table 3. Estimation of Volume of Depleted Mantle^a

Location	Width, km	Depth, km	Area, km ²
NW flank	130 ± 20	120 ± 20	15600 ± 5000
SE flank	130 ± 20	140 ± 20	18200 ± 5400

^aMeasurements are based on area of V_P/V_S image where V_P/V_S perturbation < -0.5%.

some of the most resolved upper mantle tomographic images available. This results from having a long and high-density line array aligned with most the Earth's seismicity and trending perpendicular to the major structures in the region. We also benefit from (1) the simple and well-resolved anisotropy structure that exists beneath our array [Schutt *et al.*, 1998], which allows us to estimate well and correct for the effects of anisotropy on P and S travel times, and (2) the well-resolved crustal corrections on travel time, which result from receiver function analysis constrained by active source reflection and refraction investigations [Peng and Humphreys, 1998].

[45] Even with these advantages, the seismic data by themselves are insufficient to constrain the depth distribution of structure very well. This problem is intrinsic to the data; structures of various depth distributions account for the data equally well. Good control on the depth distribution of structure is provided through the use of squeezing tests combined with plausibility arguments. We find that structure is required to depths of at least 180 km, and there is no need for structure below 190 km. When structure is imaged below 190 km, it has the form expected for streaks related to the structure imaged above 190 km. These results, combined with the geodynamic expectation that temperature and partial melt variations are minor below 190 km, argue that no significant structure exists beneath this depth. Similarly, there is no need for mantle structure above 80 km. Because the crustal structure (i.e., structure above ~40 km) is well known from other investigations, and synthetic tests suggest that we can resolve major structures in the uppermost mantle, we conclude that only modest structure can be present between 40 and 80 km.

[46] Figure 9, which is constructed under the constraint that structure is preferred to lie between 80 and 190 km, is our preferred tomographic model of V_P and V_S structure. Imaged V_P and V_S structure is quite similar in form. The amplitude of imaged structure is very large, with a strong velocity depression roughly beneath the SRP and high velocities beneath the margins of the Yellowstone swell. V_S structure resides at shallower levels than corresponding V_P structure. This result can be seen directly in the data (Figure 4), where the P delay pattern shifts with change in incidence angle by amounts greater than the S delay pattern. The high-velocity maxima seen in Figure 9 to lie inboard of the side model boundaries are thought to represent actual structure because travel time delays seen in Figure 3 are smallest for stations inboard of the array edges.

[47] The anisotropy structure and the isotropic structure do not correlate spatially (Figure 7). Anisotropy corrections to the travel time delays, at 30% and 6% of the respective P and S travel time delay RMS, are relatively small but significant. Correcting for the travel time effects of anisotropy does not significantly change the amplitude of the resulting images, although it does make the V_P image look more like the V_S .

[48] $\partial \ln V_S / \partial \ln V_P$ is resolvably greater for delayed arrivals compared to advanced arrivals (Table 1), implying the presence of partial melt in the low-velocity areas. Through the use of summary rays we produce perturbational V_P and V_S images of comparable resolution, from which a perturbational V_P/V_S image is made (Figure 12). This image confirms the greater depth of P wave structure compared to S wave structure. V_P/V_S variations are imaged at about 8% beneath the array, with a prominent V_P/V_S high beneath the SRP at about 80 km depth. A high gradient in V_P/V_S is imaged near 80–100 km depth, which is thought to be the upper reaches of partially molten mantle. Resolution tests indicate that this gradient is high; however, we have insufficient information to resolve if the gradient is as high as we show, or if it is exaggerated by the constraints used in inversion.

4.2. Physical State

[49] We conclude that the upper mantle is nearly uniformly hot and buoyant beneath the Yellowstone swell, that this mantle is significantly hotter and more buoyant than adjacent mantle, that the volume of partially molten upper mantle lies roughly beneath the SRP, and that the mantle beneath the remainder of the swell has been depleted in basalt and volatiles. By assuming the V_P/V_S perturbational contour of 0.5% represents the solidus, we infer that the volume of low V and high V_P/V_S result from the presence of up to about 1.0% basaltic melt, that the entire upper mantle swell is within ~80°K of the solidus, and that swell upper mantle averages ~200°K warmer than the surrounding mantle. Dividing the estimated volume of basalt segregated from the mantle by the volume of depleted mantle yields $5 \pm 2.5\%$ weight fraction of basalt depletion from the swell upper mantle.

4.3. Geodynamics

[50] Much of the inferred upper mantle physical state beneath the Yellowstone swell can be explained by the plume flattening models such as [Anders and Sleep, 1992]. However, these models need to be modified to account for the strong variations in imaged seismic structure [Saltzer and Humphreys, 1997]. The hot, depleted and essentially subsolidus swell mantle away from the SRP must have experienced recent melt removal which, in all likelihood, constructed the volcanic structures of the SRP crust by segregating from the mantle below. The flow of mantle up beneath the SRP and then to beneath the adjoining areas would represent convection. The only plausible source of density difference to have driven this convection is melt buoyancy [e.g., Tackley and Stevenson, 1993], which we infer continued until accumulating depletion buoyancy equaled the melt buoyancy and terminated upwelling. The system now is nearly static, though it continues to slowly spread through buoyant flattening as described by Anders and Sleep [1992].

[51] Whether or not Yellowstone is a plume that ascends under the influence of its own negative buoyancy is not resolved by our teleseismic studies, which crosses downstream of the currently active Yellowstone system. A lower mantle source for the hot spot mantle is suggested by the ~200°K excess temperature of the swell upper mantle, high He^3/He^4 [Hearn *et al.*, 1990] and lower mantle low veloc-

ities to at least as deep as 1000 km beneath the general Yellowstone area [Bijwaard *et al.*, 1998]. However, the association of Yellowstone with the Newberry hot spot (now in central Oregon) and the tectonic setting that drives upper mantle divergence [Humphreys *et al.*, 2001] suggests much of the energy driving this system derives itself from the upper mantle.

4.4. Summary

[52] To clarify how the Yellowstone hot spot material evolves as it is dragged by the North America plate, we have measured seismic velocity and use it to infer mantle physical state in a cross section across the Yellowstone Swell. We have inverted anisotropically corrected teleseismic P and S wave travel times to produce V_P and V_S images. Inversion tests show that structure is necessary between 80 and 190 km in depth, and not required outside this region. The magnitude of the V_P and V_S variations (6.2% and 11.2% respectively), and a comparison of P and S wave travel time residuals, strongly suggest the presence of partial melt under the Snake River Plain.

[53] Using summary rays, we combine the V_P and V_S images to calculate V_P/V_S . From the V_P/V_S structure, we use seismic and density constraints to estimate the physical state of the mantle in the Yellowstone Swell. We find about 1.0% melt exists under the Snake River Plain. This melt is flanked by depleted mantle that is within about 80°K of the solidus, and has had about 5% melt removed.

[54] Although the velocity and physical state structures are more accurately known, our view of the geodynamics of the Yellowstone system remains as it was set out in Humphreys *et al.* [2001] and Saltzer and Humphreys [1997].

[55] **Acknowledgments.** We would like to thank Justin Revenaugh, Karen Fischer, and an anonymous reviewer for helpful comments; also Ken Dueker for helpful advice and managing the array. This work was supported by NSF grants EAR-9628474 and EAR-9725598. Data were collected under the Program for Array Seismic Studies of the Continental Lithosphere (PASSCAL) program. D. S. wishes to thank the Carnegie Institution of Washington for postdoctoral support.

References

- Anders, M. H., and N. H. Sleep (1992), Magmatism and extension: The thermal and mechanical effects of the Yellowstone hotspot, *J. Geophys. Res.*, *97*, 15,379–15,393.
- Anders, M. H., J. W. Geissman, L. A. Piety, and T. J. Sullivan (1989), Parabolic distribution of circumeastern Snake River Plain seismicity and latest Quaternary faulting: Migratory and association with the Yellowstone hot spot, *J. Geophys. Res.*, *94*, 1589–1621.
- Bijwaard, H., W. Spakman, and E. R. Engdahl (1998), Closing the gap between regional and global travel time tomography, *J. Geophys. Res.*, *103*, 30,555–30,078.
- Dueker, K. G., and E. D. Humphreys (1990), Upper mantle velocity structures of the Great Basin, *Geophys. Res. Lett.*, *17*, 1327–1330.
- Evans, J. (1982), Compressional wave velocity structure of the upper 350 km under the eastern Snake River Plain near Rexburg, Idaho, *J. Geophys. Res.*, *87*, 2654–2670.
- Gilbert, P. F. C. (1972), Iterative methods for three-dimensional reconstruction of an object from projections, *J. Theoret. Biol.*, *36*, 105–117.
- Grand, S. P. (1994), Mantle shear structure beneath the Americas and surrounding oceans, *J. Geophys. Res.*, *99*, 11,591–11,621.
- Hales, A. L., and E. Herrin (1972), Travel times of seismic waves, in *The Nature of the Solid Earth*, edited by E. C. Robertson, pp. 172–215, McGraw-Hill, New York.
- Hammond, W. C., and E. D. Humphreys (2000), Upper mantle seismic wave velocity: Effects of realistic partial melt geometries, *J. Geophys. Res.*, *105*, 10,975–10,986.
- Hearn, E. H., B. M. Kennedy, and A. H. Truesdell (1990), Coupled variations in helium isotopes and fluid chemistry; Shoshone Geyser Basin, Yellowstone National Park, *Geochim. Cosmochim. Acta*, *54*, 3103–3113.
- Humphreys, E. D., and R. W. Clayton (1988), Adaptation of back projection tomography to seismic travel time problems, *J. Geophys. Res.*, *93*, 1073–1085.
- Humphreys, E. D., and K. G. Dueker (1994), Physical state of the western U.S. upper mantle, *J. Geophys. Res.*, *99*, 9625–9650.
- Humphreys, E. D., K. G. Dueker, D. L. Schutt, and R. B. Smith (2001), Beneath Yellowstone: Evaluating plume and nonplume models using teleseismic images of the upper mantle, *GSA Today*, *10*, 1–7.
- Isaak, D. G., O. L. Anderson, and T. Goto (1989), Elasticity of single-crystal Forsterite measured to 1700 K, *J. Geophys. Res.*, *95*, 5895–5906.
- Karato, S. (1993), Importance of anelasticity in the interpretation of seismic tomography, *Geophys. Res. Lett.*, *20*, 1623–1626.
- Keller, W. R., D. L. Anderson, and R. W. Clayton (2000), Resolution of tomographic models of the mantle beneath Iceland, *Geophys. Res. Lett.*, *27*, 3993–3996.
- Kennett, B. L. N. (1995), Seismic traveltime tables, in *Global Earth Physics: A Handbook of Physical Constants*, AGU Ref. Shelf, vol. 1, edited by T. J. Ahrens, pp. 126–143, AGU, Washington, D. C.
- Micheline, A. (1993), Testing the reliability of V_P/V_S anomalies in travel-time tomography, *Geophys. J. Int.*, *114*, 405–410.
- McKenzie, D., and M. J. Bickle (1988), The volume and composition of melt generated by extension of lithosphere, *J. Petrol.*, *29*, 625–679.
- Nolet, G. (1993), Solving large linearized tomographic problems, in *Seismic Tomography, Theory and Practice*, edited by H. M. Iyer and K. Hirahara, pp. 248–264, Chapman and Hill, New York.
- Paige, C. C., and M. A. Saunders (1982), LSQR: An algorithm for sparse linear equations and sparse least squares, *ACM Trans. Math. Software*, *8*, 43–71.
- Peng, X., and E. D. Humphreys (1998), Crustal velocity structure across the eastern Snake River Plain and the Yellowstone swell, *J. Geophys. Res.*, *103*, 7171–7186.
- Robertson, G. S., and J. H. Woodhouse (1995), Evidence for proportionality of P and S heterogeneity in the lower mantle, *Geophys. J. Int.*, *123*, 85–116.
- Saltzer, R. L., and E. D. Humphreys (1997), Upper mantle P wave velocity structure of the eastern Snake River Plain and its relationship to geodynamic models of the region, *J. Geophys. Res.*, *102*, 11,829–11,841.
- Schutt, D. L., and E. D. Humphreys (2001), Evidence for a deep asthenosphere from western United States SKS splits, *Geology*, *29*, 291–294.
- Schutt, D. L., E. D. Humphreys, and K. Dueker (1998), Anisotropy of the Yellowstone hot spot wake, eastern Snake River Plain, Idaho, *Pure Appl. Geophys.*, *151*, 443–462.
- Schutt, D. L., C. E. Leshner, and J. Pickering-Witter (2002), The effects of melt depletion on the density and seismic velocity of garnet and spinel ilherzolite, *Eos Trans., AGU*, *83*, Spring Meet. Suppl., Abstract M42A-12.
- Sparlin, M. A., L. W. Braille, and R. B. Smith (1982), Crustal structure of the eastern Snake River Plain from ray trace modeling of seismic refraction data, *J. Geophys. Res.*, *87*, 2619–2633.
- Tackley, P. J., and D. J. Stevenson (1993), A mechanism for spontaneous self-perpetuating volcanism on the terrestrial planets, in *Flow and Creep in the Solar System: Observations, Modeling, and Theory*, NATO ASI Ser. C, vol. 391, edited by D. B. Stone and S. K. Runcorn, pp. 307–322, Kluwer Acad., Norwell, Mass.
- Toomey, D. R., W. S. D. Wilcock, S. C. Solomon, W. C. Hammond, and J. A. Orcutt (1998), Mantle seismic structure beneath the MELT region of the East Pacific Rise from P and S wave tomography, *Science*, *280*, 1224–1227.
- Wolfe, C. J., I. T. Bjarnason, J. C. VanDecar, and S. C. Solomon (2002), Assessing the depth resolution of tomographic models of upper mantle structure beneath Iceland, *Geophys. Res. Lett.*, *29*(2), 1015, doi:10.1029/2001GL013657.
- York, D. (1966), Least-squares fitting of a straight line, *Can. J. Phys.*, *44*, 1079–1086.

E. D. Humphreys, Department of Geological Sciences, 1272 University of Oregon, Eugene, OR 97403-1272, USA.

D. L. Schutt, Department of Terrestrial Magnetism, Carnegie Institution of Washington, 5241 Broad Branch Road, N.W. Washington, DC 20015, USA. (schutt@dtm.ciw.edu)

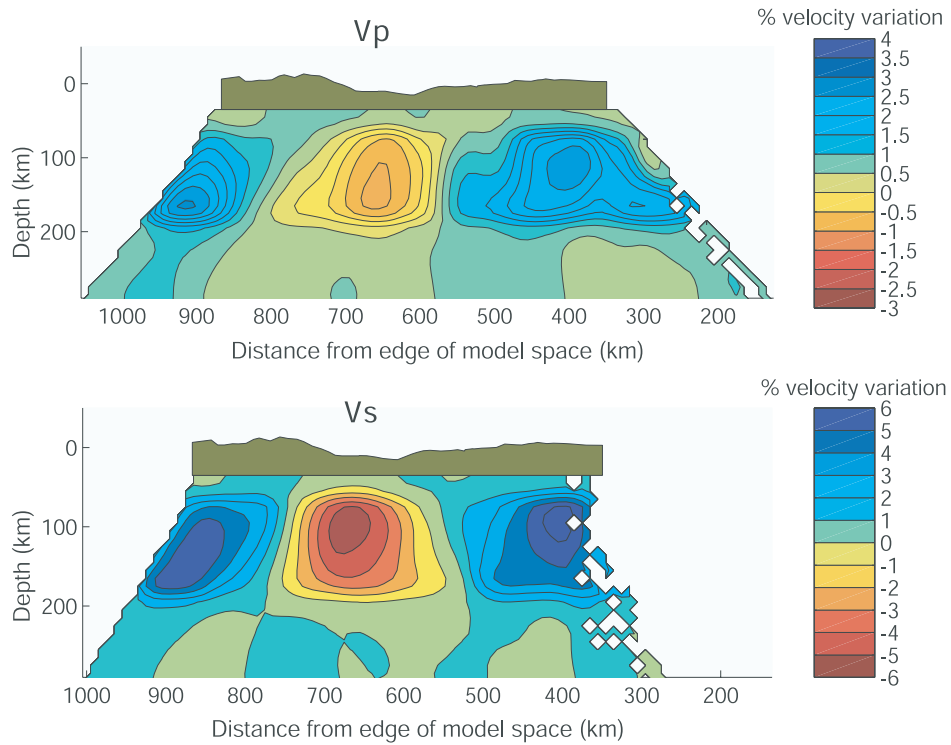


Figure 9. Best SIRT P and S images. Structure is squeezed between 80 and 190 km for 15 SIRT iterations, then squeezing is relaxed for 5 iterations. V_P varies by 6.2%, and explains 59% of the data RMS. V_S varies by 11.2%, and explains 62% of the data RMS. Exaggerated topography (at 25x) is shown above the velocity images.

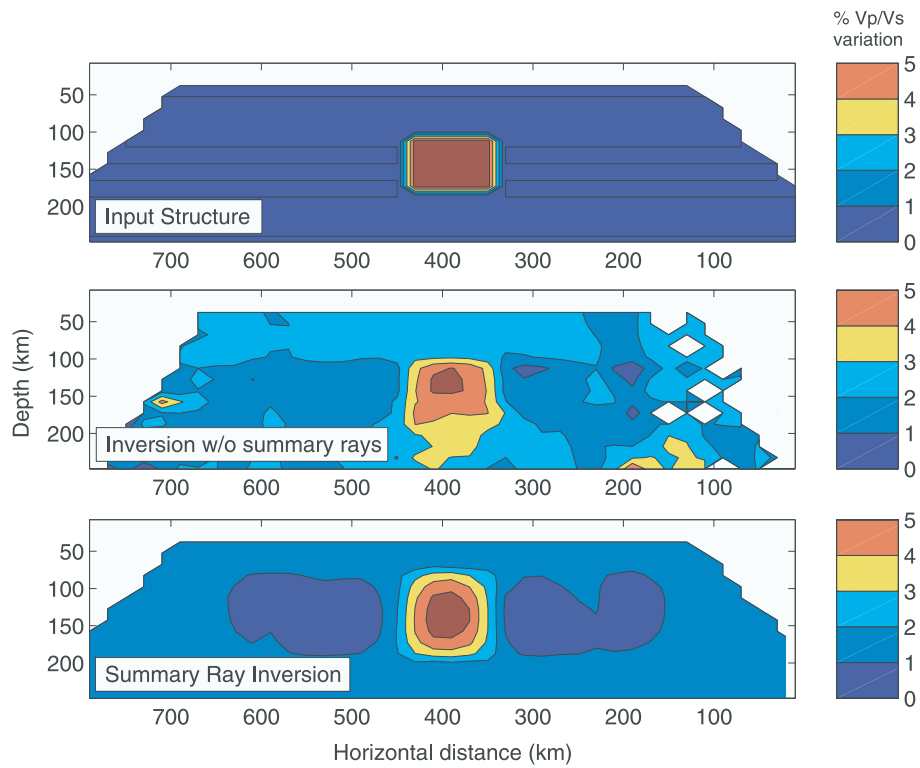


Figure 10. Synthetic V_p/V_s images. Contours at 1%. (top) Input structure. (middle) Inversion without summary rays. This suffers from spurious perturbations due to differences in P and S ray coverage. (bottom) Damped least squares inversion of summary rays. Both inversions have been multiplied by the least squares constant that best fits them to the input structure. They have also been squeezed to between 100 and 180 km.

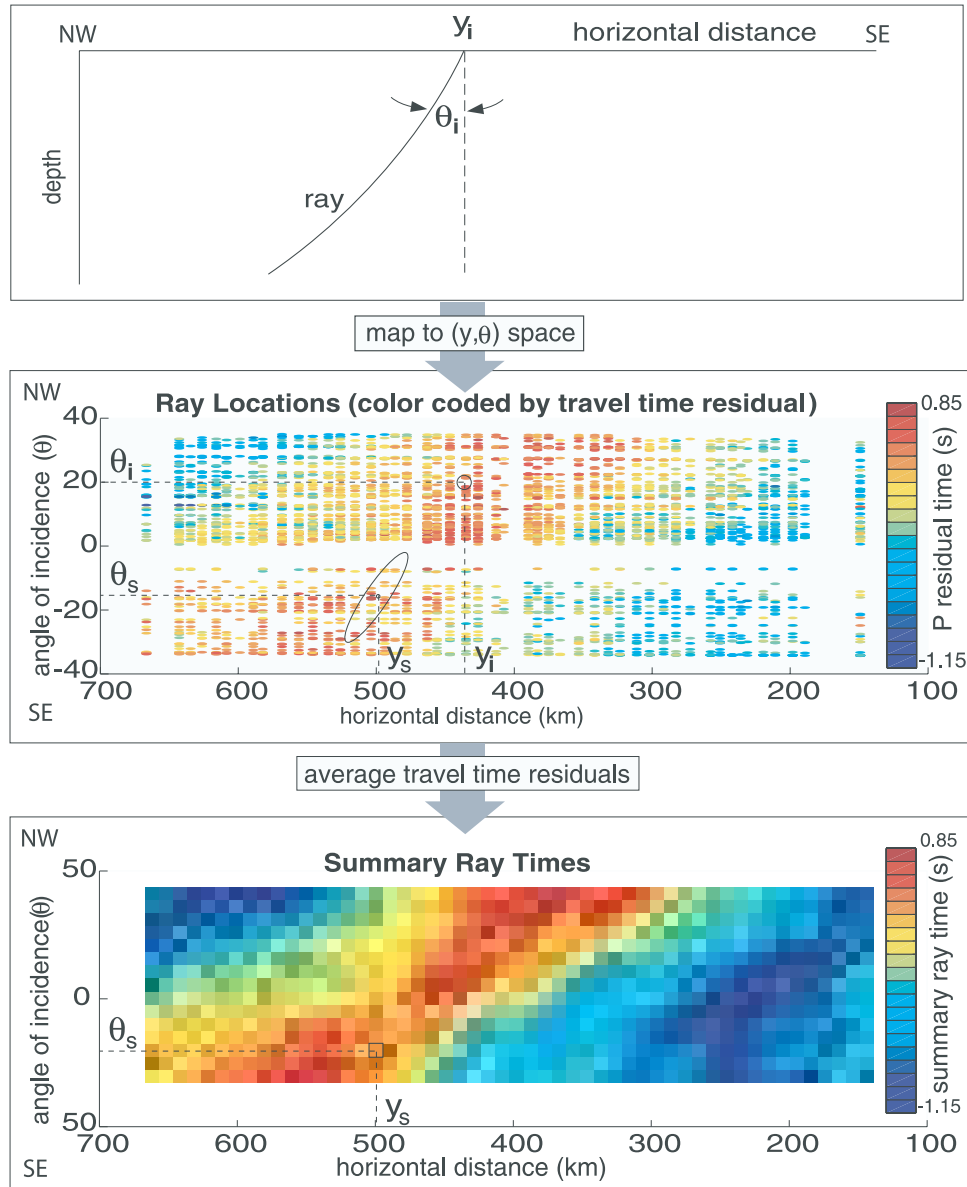


Figure 11. Summary ray travel time calculation. (top) The i th seismic ray, at surface location, y_i , and incidence angle at 30 km, θ_i . (middle) Each ray is mapped to (y, θ) space. Color indicates travel time residual for each ray. Travel times are assigned to summary rays by averaging residuals within an elliptical area around each summary ray (as shown schematically for summary ray at (y_s, θ_s)). (bottom) Delays for each summary ray.

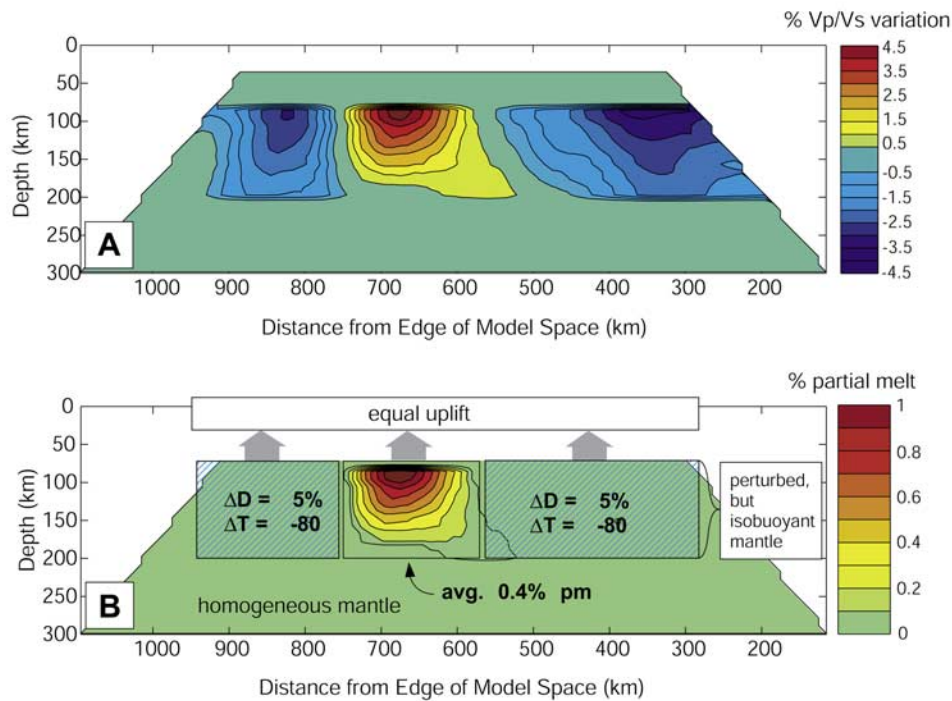


Figure 12. (a) V_p/V_s perturbation. Contours are in 0.5% intervals (the 0% contour is omitted to avoid the visual distraction of noise). Total range of perturbations is 8.0%. Assuming average V_p/V_s is 1.82, actual V_p/V_s varies from 1.75 to 1.90. To produce optimal estimation of amplitude, image has been squeezed and multiplied by a least squares constant based on damping value. (b) Physical state. On the basis of the V_p/V_s structure, we estimate the amount of partial melt to be as much as 1.0% (darkest red region), and to average 0.4% within the central rectangle. The low V_p/V_s areas are melt depleted, and we estimate these regions (approximated by the blue-lined rectangles) to have had 5% melt removal. Since the mantle is isobuoyant, uplift due to depletion and thermal variations must balance uplift due to partial melting. This suggests that the regions indicated by the blue-lined rectangles are, on average, 80° colder than the region containing partial melt.